Machine Learning Prediction on the Ground Bearing Capacity of a Rigid Footing Resting on Ground with Graded Soil Particles using Discrete Element Method

Xi Chen[1], Zongqi Liu[1,*], Zuokai Zhang[1], Chenlu Wang[1], Liusheng Cui[1], Zhikai Yan[1], Zhe Xu[1], Saif Ullah[1], Fengkai Ge[2] and Fengwei Li[3]

[1]*Key Laboratory of Urban Underground Engineering of Ministry of Education, Beijing Jiaotong University, Beijing 100044, China*

[2]*State Grid Electric Power Engineering Research Institute Co., Ltd., Beijing 100069, China*

[3]*China Railway Construction Corporation Limited, Beijing 100855, China*

Abstract: Compared to the continuum-based methods, the discrete element method (DEM) may reflect the effects of granular characteristics (such as the mean particle size d_{50}, coefficient of uniformity C_u and coefficient of curvature C_c) on the behavior of soil mass. Hence, in this work, the rolling resistance linear (RRL) contact model in combination with the circular particles in the DEM, as a simplified approach of reflecting actual shapes of soil particles, is utilized to assess the effects of granular characteristics on the ultimate bearing capacity p_u of the ground. Furthermore, a large amount of DEM simulations of ground with various granular characteristics are conducted, so that a dataset of relating the p_u to the granular characteristics for machine learning (ML) can be achieved. Based on the dataset of DEM simulations, three ML algorithms, namely multiple linear regression (MLR), artificial neural networks (ANN) and extreme gradient boosting (XGBoost), are applied to training the prediction models of p_u. The research results reveal that the footing rotations and the asymmetric failure pattern of ground in the DEM simulations are largely attributed to the granular characteristics of soil mass. For a ground composed of soil particles with larger d_{50} and larger C_u, the p_u of the ground generally tends to be higher and the thickness of developed shear band tends to be greater. For a ground composed of soil particles with larger d_{50} but smaller C_u, the asymmetric failure pattern of ground is more legible and the predicted p_u tends to be smaller. It was also found that among the investigated ML algorithms, the MLR algorithm may provide an explicit model for the p_u, while ANN and XGBoost algorithms offer higher prediction accuracy.

Keywords: Ultimate ground bearing capacity, Footing rotation, Asymmetric failure pattern, Discrete element method, Machine learning.

1. INTRODUCTION

The ultimate ground bearing capacity is a critical issue in geotechnical engineering, as it directly impacts the stability and safety of building footings. It is well known that general shear failure typically occurs for those soils with low compressibility, and this failure mode is characterized with a continuous failure surface between the footing edges and the ground surface and ground surface heave either on both sides or any one side of the footing. The influential factors of ultimate bearing capacity and failure pattern of ground can be categorized into the intrinsic types and the extrinsic types. The intrinsic types of the influential factors include the strength parameters, the anisotropy of soil mass (*e.g.* Azami *et al.*, 2009; Veiskarami and Shokoohi, 2023) and the inherent spatial variability of soil properties (*e.g.* Wu *et al.*, 2020; Krishnan and Chakraborty, 2022), while the extrinsic types of the influential factors include the types of footings (*i.e.* flexible or rigid), the geometries and the burial depths of the footings, and the characteristics of the loads

transferred to the footings (*i.e.* eccentric or inclined loading) (*e.g.* Krabbenhoft *et al.*, 2014).

Continuum-based methods have been the most popular analysis methods for geotechnical problems (Chen *et al.*, 2014). When applying the continuum-based methods to the ground bearing capacity analysis, we may find the analytical approaches such as the Prandtl-Reissner solution and Terzaghi's solution as well as the numerical approaches such as the displacement finite element method (FEM) (*e.g.* Wang *et al.*, 2019; Chen *et al.*, 2020; Tang *et al.*, 2022; Chen *et al.*, 2023; Lyu *et al.*, 2024) and finite element limit analysis (*e.g.* Shiau *et al.*, 2003; Xiao *et al.*, 2018). Some research efforts have been devoted to the asymmetric failure pattern of ground caused by random properties or anisotropy of soils and the corresponding bearing capacity using the continuum-based numerical methods (*e.g.* Loukidis *et al.*, 2008; Li *et al.*, 2015; Gao *et al.*, 2020; Fathipour *et al.*, 2022).

Alternatively, the particle-based methods such as the Discrete Element Method (DEM) can be applied to the ultimate bearing capacity analysis of ground, as these methods may present the micro-interactions and microscopic mechanisms of particles, including the
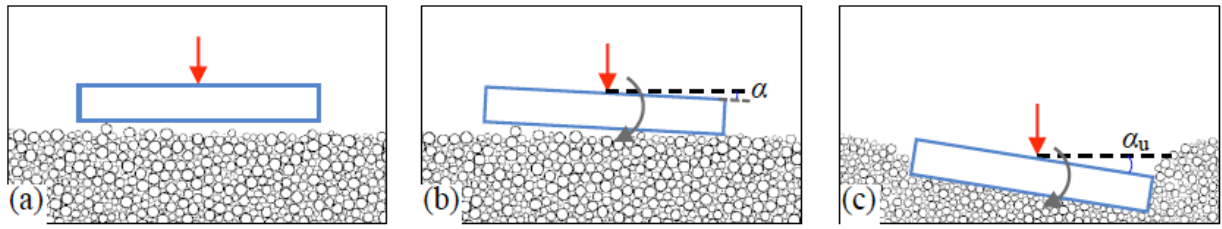
Figure 1: Settlement and rotation of a rigid footing resting on the ground composed of soil particles subjected to centric vertical load: (**a**) Before applying the load; (**b**) When the applied load is relatively small, the settlement and the rotation (α) of the footing are not significant; (**c**) When the applied load reaches the ultimate bearing capacity p_u, the footing may experience significant settlement and rotation (α_u).

movements, rotations, and contact forces of particles (*e.g.* Bhandari and Han, 2009; Fu *et al.*, 2016; Yin and Wang, 2021). Figure **1** illustrates a rigid strip footing resting on the ground composed of soil particles subjected to centric vertical load. It is readily observed that if the footing is not restrained (as depicted in Figure **1**(**a**)), it may experience not only the settlement but also the rotation (α) during the loading process (as depicted in Figure **1**(**b**) and Figure **1**(**c**)), due to the randomness of the soil particles beneath the footing. Hence, it is of practical importance to assess the footing rotation and the eventual failure pattern of the ground using DEM (*e.g.* Liu *et al.*, 2025).

In the past decade, it has been witnessed that the machine learning (ML) has become a powerful tool of extracting information, discovering potential pattern and deriving prediction model from complex data in various applications, including the prediction of the ultimate ground bearing capacity (*e.g.* Pan *et al.*, 2024; Behera and Patra, 2018; Roy and Shree, 2024). At present, several researchers have integrated ML with the DEM. Typical applications include: using ML to assist in calibrating microscopic parameters in DEM simulations (*e.g.* Wu *et al.*, 2026); employing ML to predict soil bearing capacity from in-situ borehole data, then using DEM to model and validate the ML-predicted soil bearing capacity (*e.g.* Thapa *et al.*, 2025). However, there are few studies that use DEM to perform multiple ground simulations (to generate datasets) and then use ML to train prediction models for p_u. The randomness of soil particle spatial distribution and the asymmetry of grounds are particularly suitable to be captured by DEM simulations. Furthermore, the applicability of various ML models when combined with DEM-derived ground simulation results requires further evaluation. In summary, a critical research gap remains—specifically in the integration of advanced ML techniques and the DEM simulation for analyzing ground bearing capacity problems—to enhance the accuracy of p_u predictions.

The costs of performing a large amount of in-situ tests or laboratory tests and retrieving data from these tests are generally very high, the DEM simulations for

ML predictions, however, appear to be appealing in that it may produce sufficient data economically in short time. Hence, DEM simulations are implemented here for generating the data required by ML models of ultimate ground bearing capacity. The innovation of this research mainly lies in two aspects; first, a novel modification factor χ_p is proposed to quantify the reduction of p_u induced by particle characteristics of the ground; second, based on the MLR model, an explicit expression of p_u is developed that accounts for both gradation parameters (*i.e.*, the ratio of constant footing width B to the mean particle size d_{50} (B/d_{50}), coefficient of uniformity (C_u), and coefficient of curvature (C_c)) and strength parameters (*i.e.*, friction coefficient (μ) and rolling resistance coefficient (μ_r)). The primary objectives of this study are defined as follows: **(1)** To investigate the effects of soil particle gradation characteristics (B/d_{50}, C_u, C_c) and strength parameters (μ, μ_r) on the p_u of ground, footing rotation, and asymmetric failure pattern of ground using DEM. **(2)** To propose a modification factor χ_p to correct the overestimation of p_u by continuum-based methods considering soil particle gradation effects. **(3)** To construct a dataset of p_u based on DEM simulations, then develop and compare three ML models (MLR, ANN, XGBoost) for predicting the p_u, and quantify the contribution of each soil parameter to p_u through feature importance analysis.

2. ROLLING RESISTANCE LINEAR CONTACT MODEL FOR GROUND SIMULATION

2.1. Ground Model of DEM

Experimental researches revealed that the soil particle shape (or angularity) may affect the ultimate bearing capacity and failure pattern of ground to some extent (*e.g.* Raja *et al.*, 2023), and hence simulation of the actual particle shape in DEM simulations is crucial to accurate prediction on the deformation and failure of ground. Modeling all the particles with exact shapes and positions in a geotechnical system, however, is infeasible. One type of solutions to that difficulty is to generate the soil mass in a random way by following the distribution characteristics of soil particles; the
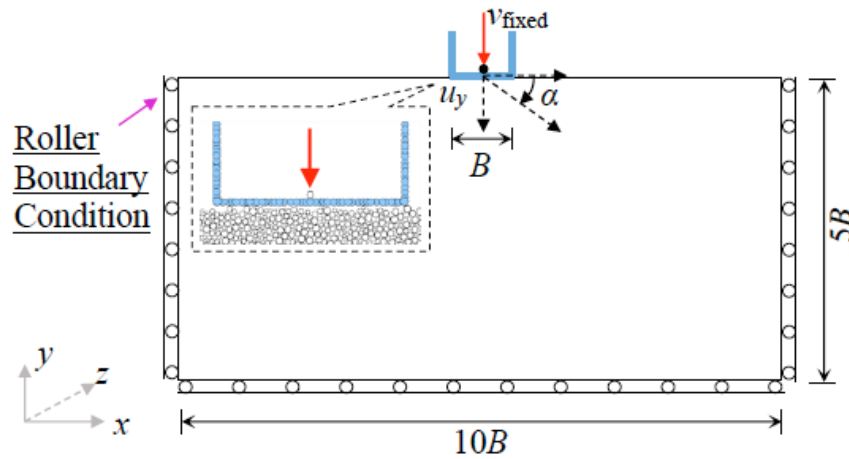
Figure 2: Ground model and the U-shaped footing clump in DEM simulation.

other type of solutions is to use a simplified model with simple particle shapes which may reflect the effects of complicated particle shapes to some extent. As one of the second type of solutions, the Rolling Resistance Linear (RRL) contact model disclosed that it may reflect the rolling resistance of angular particles by solely resorting to the circular particles (*e.g.* Yin and Wang, 2021), and hence it is employed here.

In this study, the Multi-layer with Under compaction Method (UCM) is utilized to generate the comparatively uniform and dense ground model in DEM simulations (*e.g.* Jiang *et al.*, 2003). Figure **2** illustrates the geometries and boundary conditions of a rigid footing resting on the ground of dense soil, which is a

U-shaped clump composed of pebbles. To simulate a 1:10 scale model of ground in DEM, the acceleration of gravity is set to be 10g (*e.g.* Kimura *et al.*, 1985). Those model parameters of DEM are tabulated in Table **1**, except for the gradation parameters (d_{50}, C_u, C_c) and strength parameters (μ, μ_r) of particles of ground which will be elaborated later.

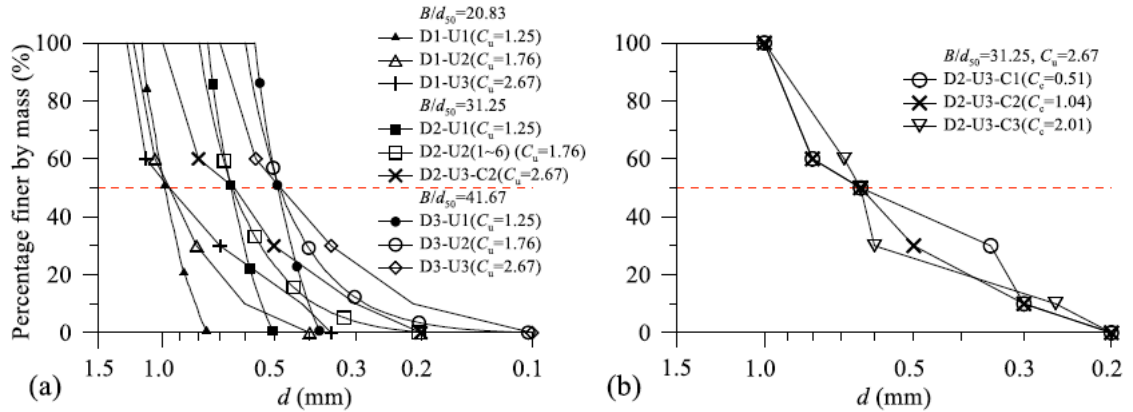### 2.2. Particle Parameters of Ground Model in DEM

The influence of particle size on the ground bearing capacity can be indirectly reflected by the shear band thickness, since the shear band thickness is generally proportional to the particle size d_{50} (*e.g.* Toyosawa *et al.,* 2013). Utilization of only a single particle size

Table 1: Model Parameters in 2D Simulations of DEM

Category	Symbol	Meaning (unit)	Value
Model geometry	B	Width of the footing (mm)	20
RRL contact model	E^*	Effective modulus of deformability (MPa)	15
	k^*	Normal-to-shear stiffness ratio	1.5
Soil particle	ζ_s	Local damping coefficient	0.7
	ρ_s	Density (kg/m^3)	2700
	n_{tar}	Target porosity	0.13
Pebble of the clump	$d_{cp,min}$	Minimum diameter (mm)	0.78
	$d_{cp,max}$	Maximum diameter (mm)	0.92
	ζ_{cp}	Local damping coefficient	0.7
	ρ_{cp}	Density (kg/m^2)	2700
Loading particle	v_{fixed}	Fixed loading velocity (mm/s)	0.5
	d_p	Diameter (mm)	0.72
	ζ_p	Local damping coefficient	0.7
	ρ_p	Density (kg/m^3)	2700
	cb_{ten}	LCB contact model tensile strength (N)	10^{300}
	cb_{shear}	LCB contact model shear strength (N)	10^{300}

Table 2: Particle Parameters for Ground Bearing Capacity Analysis of DEM Simulations (B=20mm)

Test group		B/d_{50}	C_u	C_c	d_{min} (mm)	d_{max} (mm)	d_{mdn} (mm)	μ	μ_r	Number of particles
D1	D1-U1	20.83	1.25	1.01	0.76	1.14	0.95			24249
	D1-U2		1.76	1.04	0.40	1.20	0.80			31921
	D1-U3		2.67	1.05	0.35	1.25	0.80	0.5	0.5	43585
D2	D2-U1	31.25	1.25	0.98	0.50	0.76	0.63			55065
	D2-U2(1)									
	D2-U2(2)							0.3	0.3	
	D2-U2(3)		1.76	1.09	0.20	0.80	0.50		0.5	79330
	D2-U2(4)							0.5	0.1	
	D2-U2(5)								0.3	
	D2-U2(6)							0.7	0.5	
	D2-U3-C1			0.51						108168
	D2-U3-C2		2.67	1.04	0.20	1.00	0.60			90812
	D2-U3-C3			2.01						92640
D3	D3-U1	41.67	1.25	0.99	0.38	0.56	0.47	0.5	0.5	100019
	D3-U2		1.76	1.03	0.10	0.60	0.35			154411
	D3-U3		2.67	1.04	0.10	0.70	0.40			199639

Figure 3: Particle gradation curves of granular soils in the DEM simulations: (**a**) Test groups of D1, D2-U1, D2-U2(1~6), D2-U3-C2 and D3; (**b**) Test groups of D2-U3.

parameter (d_{50}), however, cannot fully reflect the effects of complex characteristics (such as the span and continuity) of soil particle gradation. It is well known that the real soils may more or less possess certain span of particles, so the voids formed by large particles may be filled with the small particles, contributing a lot to the interlocking among the particles. Hence, it is necessary to study the impact of more detailed gradation parameters on the ground bearing capacity. The coefficient of uniformity C_u ($=d_{60}/d_{10}$) describes the span of the gradation, while the coefficient of curvature C_c ($=d_{30}^2/(d_{10} \times d_{60})$) signifies the continuity of the gradation. A total of 16 test groups, as tabulated in Table **2**, are designed by changing B/d_{50}, C_u, C_c, μ and μ_r. It is noted that the median particle size

d_{mdn} in Table **2** is the average value of the maximum and minimum particle sizes (*i.e.* $d_{mdn} = (d_{min} + d_{max})/2$). Figure **3**(**a**) shows the particle gradation curves for the test groups of D1, D2-U1, D2-U2(1~6), D2-U3-C2, and D3 in Table **2**, while Figure **3**(**b**) illustrates the three particle gradation curves of D2-U3 in Table **2** by fixing B/d_{50} and C_u but varying C_c.

It is not difficult to imagine that as the ground in DEM simulation is composed of randomly distributed particles, it generally presents the asymmetric failure pattern (or shear bands) at the failure stage, and even for the same test group, the calculated p_u of ground with soil particles created by different random seeds may vary in a range of $[p_{u,min}, p_{u,max}]$. To demonstrate this phenomenon, 27 DEM tests due to different
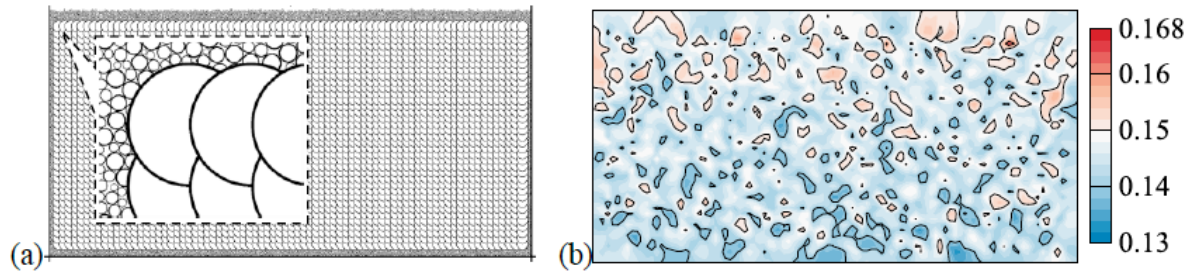
Figure 4: (**a**) Layout of measurement circles in the ground of test group D2-U2(1); (**b**) Initial porosity field of the entire ground of test group D2-U2(1).

random seeds are created for each test group, so a total of 432 (=16×27) DEM tests on the ultimate bearing capacity of ground are carried out.

3. ANALYSIS ON ULTIMATE BEARING CAPACITY OF GROUND USING DEM SIMULATIONS

3.1. Ultimate Ground Bearing Capacity Results of DEM Simulations

By arranging the measurement circles in DEM simulations (as shown in Figure **4**(**a**)), the porosity of the solution domain covered by the measurement circles can be attained. Figure **4**(**b**) illustrates the porosity field calculated by the Kriging interpolation method for the ground model of test group of D2-U2(1). It is observed that there is a general increasing trend of the porosity of ground from the deep layer to the top layer and the particle distribution in each layer of the ground is more or less asymmetric, conforming to realistic grounds.

Evidently, the randomness of the particle distribution of ground may definitely contribute a lot to the characteristics of the failure pattern as well as the ultimate bearing capacity p_u of ground. In addition, it is interesting to investigate the rotation angle α (in degrees) (with the positive value signifying the clockwise rotation) of the footing during the loading process, so the relationship between the ultimate rotation angle α_u and the corresponding p_u can be evaluated. To fulfill the purpose, a total of 432 (=16 test groups × 27 random seeds/test group) DEM tests on the ultimate ground bearing capacity are carried out, so 432 pairs of (p_u, α_u) are calculated. Furthermore, the 3σ method is applied to these 432 pairs of (p_u, α_u), and 5 outliers (1 in D2-U2(1), 3 in D2-U2(6) and 1 in D2-U3-C3) are removed, so 427 pairs of (p_u, α_u) are utilized for training the ML models.

Figure **5** illustrates two footing bottom pressure-settlement (p-u_y/B) curves obtained from the test group of D2-U2(1) characterized by a prominent peak value (p_u) and a post-peak strain softening stage. It is noteworthy that among 27 curves produced from different random seeds in the test group of D2-U2(1), the two curves correspond to the one with the minimum

peak value ($p_{u,min}$=416.7kPa) and the one with the maximum peak value ($p_{u,max}$=559.4kPa), respectively. After removing the outliers, 26 pairs of (p_u, α_u) from the test group of D2-U2(1) are provided in Table **3**.
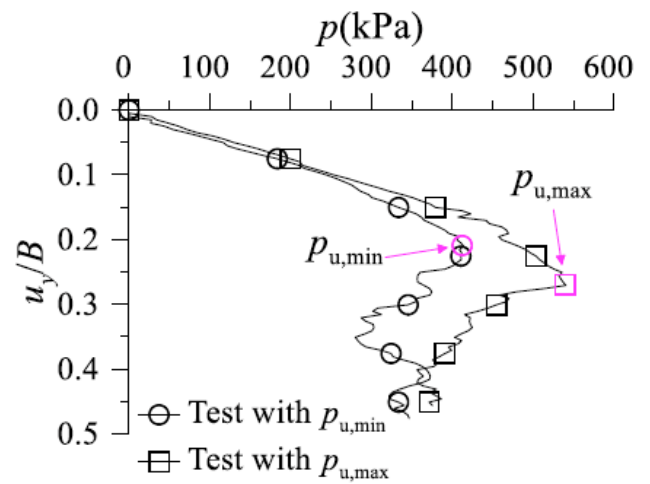

Figure 5: p-u_y/B curves with $p_{u,min}$ and $p_{u,max}$ from 27 different random seeds in DEM simulations for test group D2-U2(1).

Table 3   Results of (p_u, α_u) Obtained from the Test Group of D2-U2(1)

Test no. Due to Random Seed	D2-U2(1)	
	p_u (kPa)	α_u (°)
1	515.3	2.5
2	434.3	4.0
3	488.7	0.8
4	517.5	2.1
5	504.0	2.5
6	476.9	−3.1
7	512.7	−2.8
8	501.1	4.4
9	523.8	−1.8
10	495.4	−2.4
11	448.9	−3.4
12	556.8	−3.0
13	448.1	4.2

14	<u>474.4</u>	−7.3(outlier)
15	553.8	2.1
16	432.3	−3.2
17	559.4	−2.7
18	511.4	−1.0
19	474.7	−5.1
20	490.5	−3.8
21	507.8	2.3
22	505.1	3.0
23	530.2	1.2
24	416.7	−1.0
25	449.0	3.7
26	535.3	2.3
27	455.3	−2.5

The statistics (including the minimum value, the maximum value, the average value, and standard deviation) of the particle gradation parameter (B/d_{50}, C_u, C_c) and strength parameters (μ, μ_r) of 427 DEM tests are summarized in Table **4**. To measure the linear correlation between various parameters and p_u, the Pearson correlation coefficient ρ_c can be utilized:

$$\rho_c = \frac{\text{Cov}(X,Y)}{\sqrt{D(X)}\sqrt{D(Y)}} = \frac{\sum_{i=1}^{n_v}(X_i - \bar{X})(Y_i - \bar{Y})}{\sqrt{\sum_{i=1}^{n_v}(X_i - \bar{X})^2}\sqrt{\sum_{i=1}^{n_v}(Y_i - \bar{Y})^2}} \tag{1}$$

where X_i and Y_i denote the ith of the total n_v values of X and Y, respectively. It is known from Table **4** that there is certain negative correlation between B/d_{50} and p_u, while other parameters are more or less positively correlated with p_u. Among the parameters positively

Table 4:   Statistics of the Particle Parameters for 427 DEM Tests

Category	Symbol	Meaning	Min value	Max value	Average Value	Standard Deviation	ρ_c (with p_u)
Gradation parameter	B/d_{50}	Dimensionless mean particle size (B=20mm)	20.83	41.67	31.25	6.42	−0.15
	C_u	Coefficient of uniformity	1.25	2.67	1.95	0.52	0.39
	C_c	Coefficient of curvature	0.51	2.01	1.08	0.27	0.05
Strength parameter	μ	Friction coefficient	0.30	0.70	0.49	0.08	0.74
	μ_r	Rolling resistance coefficient	0.10	0.50	0.45	0.11	0.65

Table 5:   Statistics of p_u for 427 Tests of DEM

Test group			Min value ($p_{u,min}$)	Max value ($p_{u,max}$)	Average value ($\overline{p_u}$)	Standard deviation	ρ_c (with |αu|)	X_p
D1	D1-U1		364.81	552.41	429.44	48.07	−0.43	0.660
	D1-U2		442.49	650.69	538.34	49.72	−0.53	0.680
	D1-U3		487.88	632.84	571.99	35.25	−0.50	0.771
D2	D2-U1		313.44	447.98	386.19	31.64	−0.60	0.700
	D2-U2	D2-U2(1)	416.69	559.43	494.04	39.00	−0.27	0.745
		D2-U2(2)	161.89	187.29	171.75	6.82	−0.05	0.864
		D2-U2(3)	192.13	233.25	213.93	10.17	0.01	0.824
		D2-U2(4)	167.99	197.77	180.80	7.45	0.03	0.849
		D2-U2(5)	297.26	387.88	347.70	22.80	0.16	0.766
		D2-U2(6)	638.26	785.05	704.31	32.32	−0.42	0.813
	D2-U3	D2-U3-C1	431.18	574.79	499.74	38.41	−0.33	0.750
		D2-U3-C2	452.77	588.67	513.20	29.37	−0.40	0.769
		D2-U3-C3	447.58	587.12	519.60	33.47	−0.45	0.762
D3	D3-U1		309.92	412.71	366.41	22.36	−0.51	0.751
	D3-U2		404.17	530.29	473.66	26.49	−0.50	0.762
	D3-U3		459.95	562.10	493.84	23.87	−0.30	0.818
All			161.89	785.05	429.29	144.84	/	0.206

correlated with p_u, p_u has the largest positive correlation with μ (ρ_c=0.74), while p_u has the smallest positive correlation with C_c (ρ_c=0.05).

3.2. Effects of Particle Gradation Parameters on Ultimate Ground Bearing Capacity

The statistics of p_u for 427 DEM tests are tabulated in Table **5**, and the curves of $p_{u,min}$, $p_{u,max}$, and average value of p_u (*i.e.* $\overline{p_u}$) for each test group are plotted in Figure **6**. Figure **6** delineates the variation ranges of p_u ([$p_{u,min}$, $p_{u,max}$]) for all test groups; overlaps between these ranges across different parameters shall be

attributed to the uncertainty of p_u caused by the randomness of soil particles. The general trends of p_u with different parameters, however, can still be identified (particularly from the variations of $\overline{p_u}$). It is observed from Figure **6**(a) that given a constant C_u, $\overline{p_u}$ increases with the increase of d_{50} (or the decrease of B/d_{50}), while from Figure **6**(b) it is seen that given a constant d_{50}, $\overline{p_u}$ increases with the increase of C_u, but the increasing rate when C_u<1.76 is greater than that when C_u>1.76. It is observed from Figure **6**(c)-(d) that $\overline{p_u}$ increases with the increase of C_c, μ or μ_r.
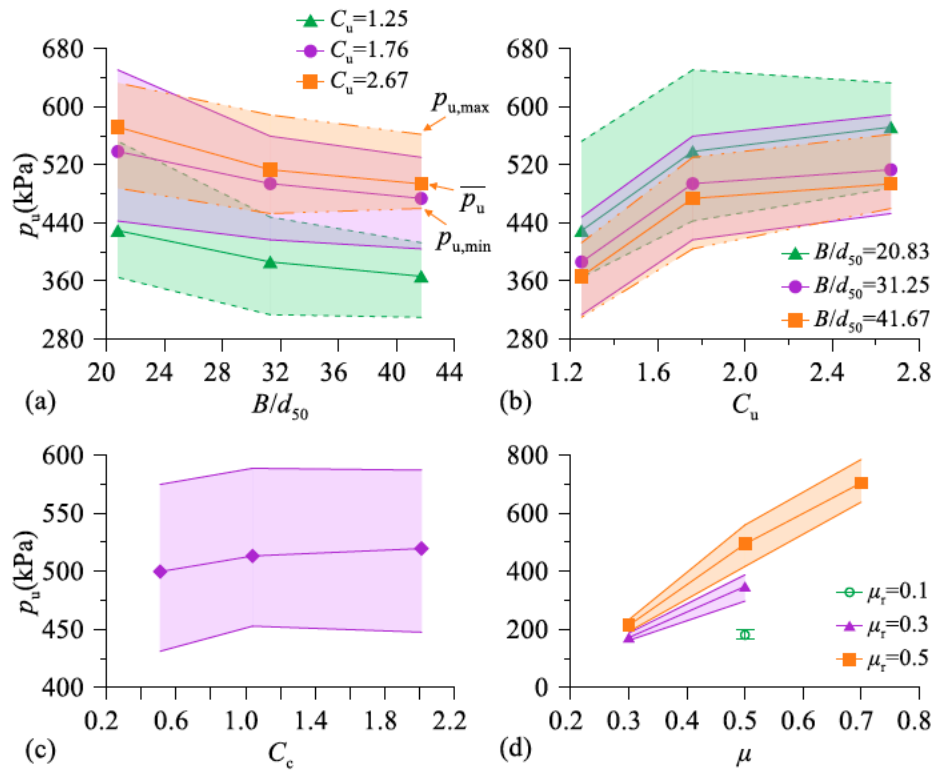

Figure 6: Variations of $p_{u,min}$, $p_{u,max}$, and $\overline{p_u}$: (**a**) with B/d_{50} ($\mu=\mu_r$=0.5); (**b**) with C_u ($\mu=\mu_r$=0.5); (**c**) with C_c (B/d_{50}=31.25, C_u=2.67, $\mu=\mu_r$=0.5); (**d**) with μ (B/d_{50}=31.25, C_u=1.76).
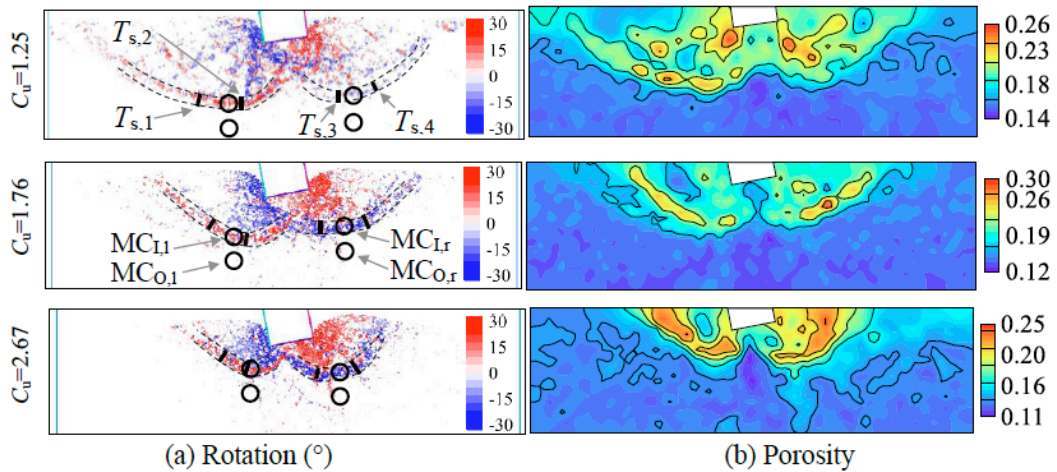

Figure 7: Contours of different fields of the upper half of the ground for illustrating the evolution of shear bands with C_u (B/d_{50}=31.25 and u_y/B=0.4): (**a**) Particle rotation (°) with absolute rotation angles greater than 10°; (**b**) Porosity.
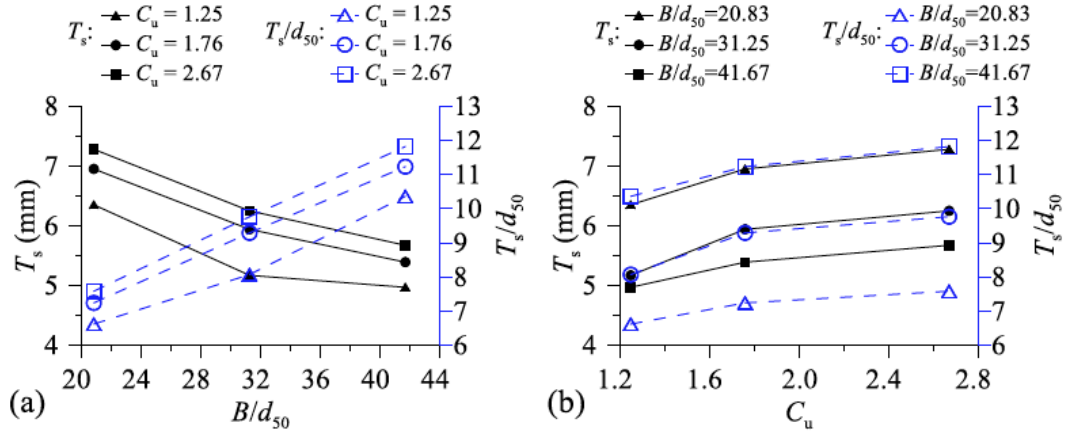
Figure 8 Variations of shear band thickness T_s (T_s/d_{50}) with: (a) B/d_{50}; (b) C_u.

Figures **8** plot the particle rotation fields (in degrees) (with the positive value representing the counterclockwise rotation of particle) and porosity fields of the upper half of the ground varying with C_u given u_y/B=0.4 and B/d_{50}=31.25. Porosity fields in Figure **8**(**b**) are obtained by the measurement circles arranged in an array layout similar to those elaborated in Figure **4**(**a**). Because the ground is composed of compacted dense soils, the general shear failure characterized with legible slip surfaces can be observed at the final failure stage of ground. It is clearly seen that the increases of the particle rotation angle and the porosity within the region of shear band are more pronounced than those outside the region of shear band. It is also noted that compared to the porosity field, it shall be easier and more consistent to measure the thickness of shear band (T_s) from the rotation field (*e.g.* Chen *et al.*, 2022; Liu *et al.*, 2024). To measure T_s, the left branch of shear band is measured at two positions for the thickness $T_{s,1}$ and $T_{s,2}$, and similarly the right branch of shear band is measured at two positions for the thickness $T_{s,3}$ and $T_{s,4}$. Hence, the shear band thickness T_s can be calculated as the average value of the measured four thicknesses, that is, T_s=($T_{s,1}$+$T_{s,2}$+$T_{s,3}$+$T_{s,4}$)/4, whose dimensionless definition is T_s/d_{50}. Figure **8**(**a**) shows the curves of T_s (T_s/d_{50}) varying with B/d_{50} (d_{50}) for constant C_u, while Figure **8**(**b**) shows the curves of T_s (T_s/d_{50}) varying with C_u for constant B/d_{50} (d_{50}). From Figure **8**(**a**), it is seen that for a constant C_u, T_s generally increases with the increase of d_{50}, but T_s/d_{50} decreases with the increase of d_{50}. From Figure **8**(**b**), it is observed that T_s (T_s/d_{50}) generally increases with the increase of C_u for a constant B/d_{50} (d_{50}). For a constant B/d_{50} (d_{50}), however, the variation of T_s/d_{50} with C_u is insignificant. Hence, it is concluded that the ratio of T_s/d_{50} is mainly dominated by the mean particle size d_{50} instead of other gradation parameters such as C_u and C_c, conforming to the experimental observations of Rattez *et al.* (2022). A large C_u, nevertheless, only contributes slightly to T_s

since the enhanced interlocking of particles in different sizes may mildly lead to the thickness of shear band. To investigate the effect of C_u, the force chain network of contacts of particles for the local region around $MC_{I,r}$ (within the shear band) and the local region around $MC_{O,r}$ located 7mm below $MC_{I,r}$ (outside the shear band) as shown in Figure **7** are depicted in Figure **9**, and the thickness of the force chain signifies the relative magnitude of the contact force. From Figure **9**, it is clearly seen that compared to the force chain networks at the local region around $MC_{O,r}$, those at the local region around $MC_{I,r}$ are characterized with more evident difference in the thicknesses of force chains and the directionality of the several major force chains is basically perpendicular to the slip surface. In addition, it is also seen that no matter at which measurement circle, the difference in the thicknesses of force chains tends to be more prominent with the increase of C_u.

To further observe the force chain network quantitatively, the coordination number N_c, which represents the average number of active contacts per body (where a body can be either a ball or a clump), is defined as

$$N_c = \sum_{i=1}^{N_b} n_i^c \bigg/ N_b \tag{2}$$

where the summation is taken over the N_b bodies whose centroids are located in the measurement circle, and n_i^c is the number of active contacts of other bodies with the ith body. During the loading process of the footing, the variations of N_c at 4 measurement circles (as shown in Figure **7**) for different C_u are measured and plotted in Figure **10**. From Figure **10**, it can be observed that for all cases, the values of N_c at u_y/B=0 are close to 4.10 before the loading. However, it is worth underscoring three interesting observations on N_c. First, during the loading process of the footing, N_c decreases rapidly at the initial stage of $u_y/B \leq 0.1$ and decreases mildly and maintain at a relatively constant
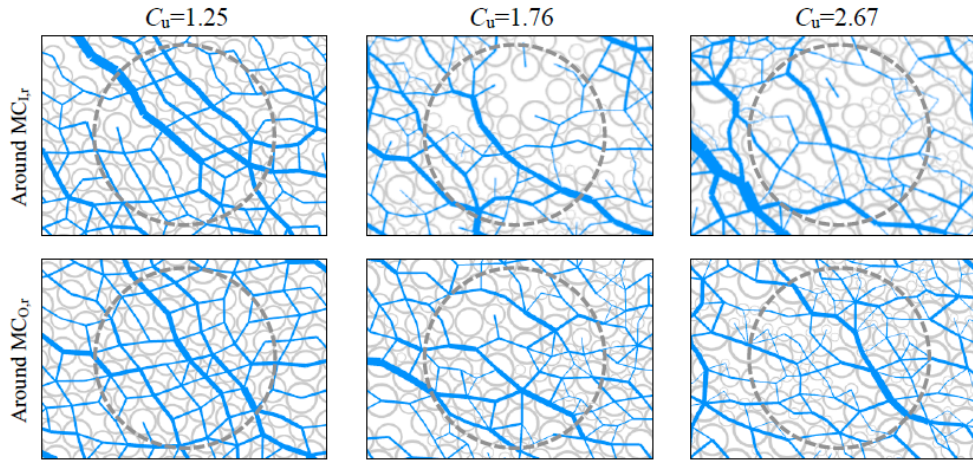
Figure 9: Force chain networks at the local regions around $MC_{I,r}$ and $MC_{O,r}$ for different C_u given u_y/B=0.4.
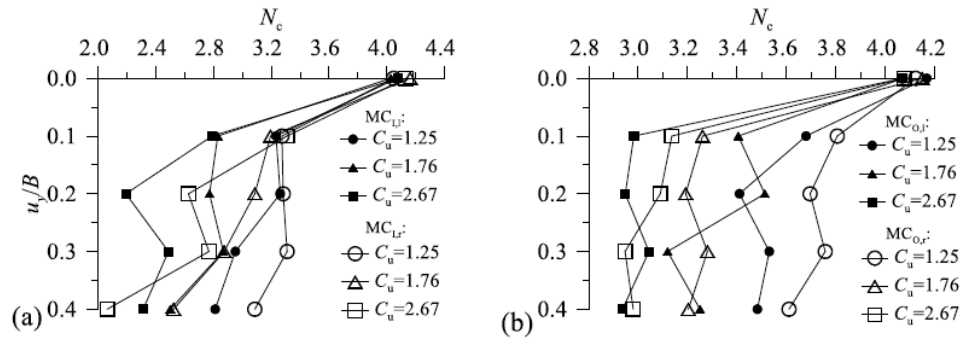

Figure 10: Variation of coordination number N_c during the loading process of the footing for different C_u at: (a) measurement circles inside the shear band ($MC_{I,l}$ and $MC_{I,r}$); (b) measurement circles outside the shear band ($MC_{O,l}$ and $MC_{O,r}$).

value at the stage of u_y/B>0.1. Second, when the ground is loaded to the failure stage (*i.e.* u_y/B=0.4), N_c calculated from MC_I within the shear band are evidently smaller than those calculated from MC_O outside the shear band, disclosing the shear dilatancy behavior in shear band region. Third, for any measurement circle (*i.e.* $MC_{I,l}$, $MC_{I,r}$, $MC_{O,l}$ or $MC_{O,r}$) located within or outside the shear band, N_c reduces with the increase of C_u from 1.25 to 2.67, implying that the shear dilatancy behavior at the ground failure shall be more prominent for a larger C_u.

The coefficient of curvature C_c represents the curvature of the particle gradation curve and the continuity of the particle gradation. The DEM simulation

results of D2-U3 reveals that the thickness of shear band is insensitive to C_c. Furthermore, by observing the DEM simulation results of D2-U2, it is found that when setting a combination of large μ and large μ_r, the failure mode and the shear band of ground appear to be legible. As a result, only the effects of B/d_{50} and C_u on the asymmetry and ultimate bearing capacity of ground (with $\mu = \mu_r = 0.5$) are examined, while C_c, μ, and μ_r are not considered any more.

3.3. Effects of Footing Rotation on Ultimate Ground Bearing Capacity

It is not difficult to imagine that the randomness of soil particles of ground may lead to more or less
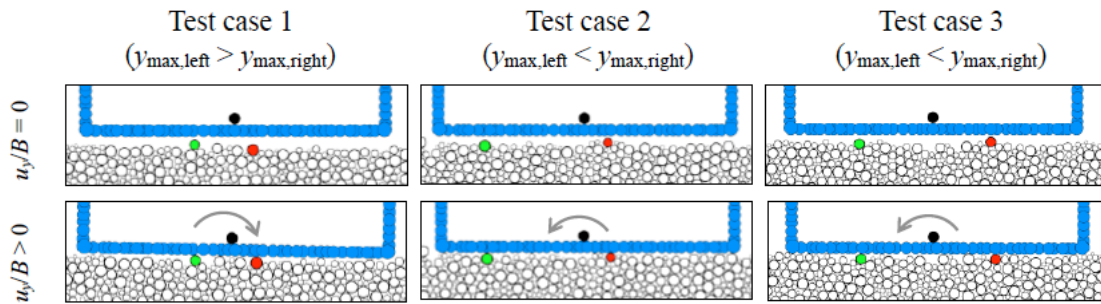

Figure 11: Location of the particle on the left half with $y_{max,left}$ (in green color) and the particle on the right half with $y_{max,right}$ (in red color) just below the footing bottom as well as initial footing rotation caused by inequality of $y_{max,left}$ and $y_{max,right}$.

rotation of the footing, which may further affect the ultimate ground bearing capacity. To assess the effects of footing rotation, three test cases generated by random seeds from the test group D2-U2(1) are illustrated in Figure **11**, in which $y_{max,left}$ and $y_{max,right}$ are defined for the particles at the left half and at the right half of ground with the maximum coordinate of y, respectively. For the test case 1, $y_{max,left} > y_{max,right}$ and the footing tends to rotate in a clockwise direction, while for the test case 2 or 3, $y_{max,left} < y_{max,right}$ and the footing tends to rotate in a counterclockwise direction. Hence, the initial rotation direction of footing can be readily determined by comparing $y_{max,left}$ with $y_{max,right}$. It shall be emphasized here, however, that the initial rotation direction of footing may not be the final rotation direction of footing (at the ground failure stage), although they are consistent in some cases.
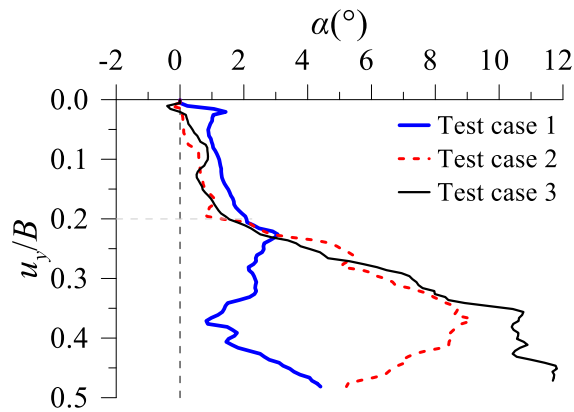

Figure 12: Three curves of footing rotation angle α (with the positive value signifying the clockwise rotation) versus settlement u_y/B.

Corresponding to the three test cases, the footing rotation angle-settlement (α-u_y/B) curves are plotted in

Figure **12**. It is evidently observed that for the test case 1, the rotation of footing is always at the clockwise direction, while for the test case 2 or 3 the footing initially rotates in the counterclockwise direction and then turns to the clockwise direction. Furthermore, based on the curves in Figure **12**, it is seen that before u_y/B=0.2, the rotation angle is less than 2°, indicating that during the loading process before u_y/B=0.2, the ground may mainly undergo the compaction of soils but with small rotation of footing, but after that, significant rotation of footing accompanying with the footing settlement can be observed. This phenomenon can be further validated through the rotation fields of particles of ground near the footing in Figure **13**.

By referring to Figure **12** and Figure **13**, the failure pattern of ground and the corresponding behavior of footing can be generally categorized into two types. That is, the type I, in which we may find the test case 1, is characterized with the near-symmetric failure pattern and small rotation of footing, while the type II, in which we may find the test cases 2 and 3, is characterized with the evidently asymmetric failure pattern and large rotation (for example, 5°) of footing. The ultimate ground bearing capacities for test cases 1, 2 and 3 are 515.3 kPa, 488.7 kPa and 504.0 kPa, respectively, so the ultimate ground bearing capacity for the test case 1 is about 5.44% higher than that of test case 2 and about 2.24% higher than that of test case 3. As a result, it may be postulated that small rotation of footing and symmetric failure pattern of ground shall be beneficial to the ultimate ground bearing capacity. To further verify this opinion, the plots similar to those in Figure **13** are replotted in Figure **14**, but with the rotation of footing completely restricted for three test cases. From Figure **14**, it is clearly observed that, compared to the
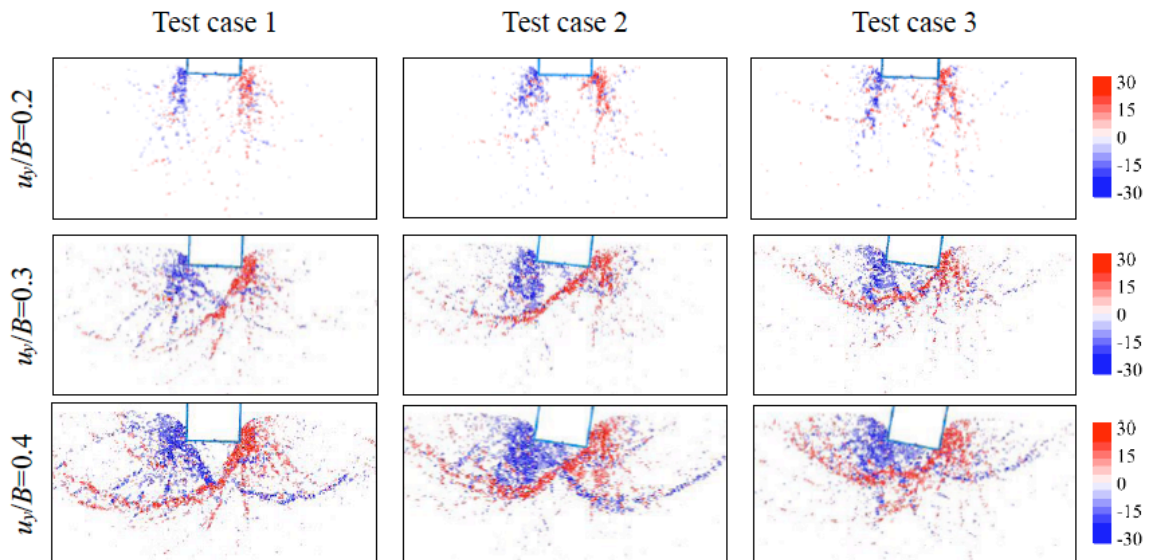

Figure 13: Rotation fields of particles with absolute rotation angles greater than 10° for the ground near the footing (without its rotation being restricted) for different footing settlements.
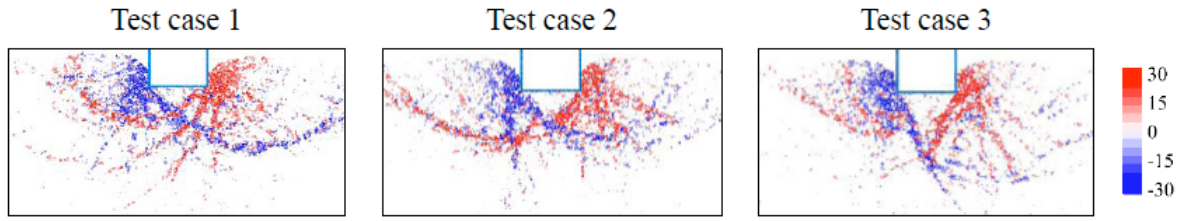
Figure 14: Rotation fields of particles with absolute rotation angles greater than 10° for the ground near the footing (with its rotation being restricted) for different footing settlements (u_y/B=0.4).
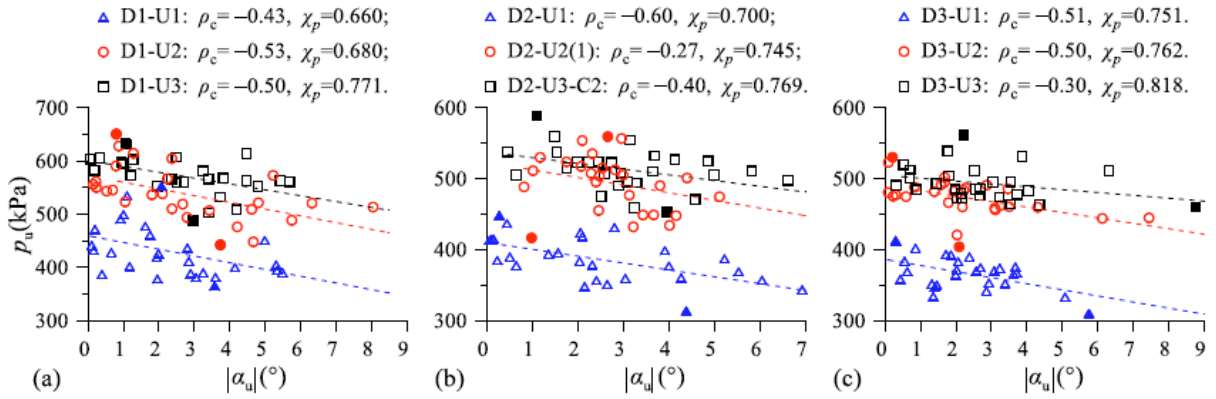

Figure 15: Linear fitting of p_u and $|\alpha_u|$: (**a**) Test groups of D1; (**b**) Test groups of D2-U1, D2-U2(1), and D2-U3-C2; (**c**) Test groups of D3.

cases with the footing rotation being unrestricted, the failure pattern of the ground in test case 2 is more symmetric compared to the test case 3, which shall be attributed to the randomness of soil particles of ground. By restricting the rotation of the footing, the p_u in all three test cases can be increased. To be specific, the p_u for test cases 1, 2, and 3 can be increased to 530.1 kPa, 517.0 kPa, and 527.8 kPa, achieving the improvements of 2.87%, 5.79%, and 4.72%, respectively. These results suggest that the restriction of footing's rotation may enhance the ultimate ground bearing capacity for a footing.

As emphasized above, the footing rotation even under centric vertical load is caused by randomness of soil particles of ground in DEM simulations, so the failure pattern of ground accompanied with the footing rotation may also present more or less asymmetry. Consequently, the relationship between p_u and the absolute value of α_u (*i.e.* $|\alpha_u|$) is investigated for all test groups, and linear fitting is carried out on all the data of p_u and $|\alpha_u|$ with the Pearson correlation coefficient ρ_c, as given in Table **5**. According to Table **5**, it is also seen that small μ or μ_r (<0.5) may lead to small absolute value of ρ_c (≤0.16), implying that there exists an indefinite linear correlation between p_u and $|\alpha_u|$. Furthermore, the linear fitting is applied to p_u and $|\alpha_u|$ calculated from test groups D1, D2-U1, D2-U2(1), D2-U3-C2 and D3, as shown in Figure **15**, in which the symbols with the maximum value $p_{u,max}$ and the minimum value $p_{u,min}$ are particularly emphasized as

the solid symbols. From Figure **15**, it is seen that there is certain degree of negative linear correlation between p_u and $|\alpha_u|$. In other words, a greater footing rotation $|\alpha_u|$ corresponds to a lower p_u, and for the investigated test groups the Pearson correlation coefficient ρ_c between p_u and $|\alpha_u|$ varies from –0.60 to –0.27, indicating that the potential rotation of footing shall be adequately considered in the footing design. The maximum overestimation ratio of p_u can be calculated as

$$R_p = \left(p_{u,max} - p_{u,min} \right) / p_{u,min} \tag{3}$$

To be conservative in practical design, the effects of particle gradation of granular soil of ground shall be adequately considered in the calculation of p_u, and hence a heuristic modification factor χ_p is introduced here as:

$$\chi_p = p_{u,min} / p_{u,max} \tag{4}$$

with which, the ultimate bearing capacity of ground in design may be calculated by

$$p_{u,design} = \chi_p \, p_{u,continuum} \tag{5}$$

where $p_{u,continuum}$ is the ultimate bearing capacity of ground calculated based on the continuum-based methods. The χ_p can be interpreted as the ratio of the p_u of the ground when the asymmetry induced by the random distribution of particles is maximized

Table 6:   Uncertainties of each Regression Coefficient in the MLR Model

Parameter	Point Estimate (PE)	Standard Error (SE)	Relative Error (RE)
B/d_{50}	0.0035	0.0006	17.14%
C_u	0.0585	0.0087	14.87%
Constant term (or intercept)	0.5188	0.0255	4.92%

(corresponding to $p_{u,min}$ in this study) to that when the asymmetry is minimized (corresponding to $p_{u,max}$). To a certain extent, χ_p reflects the maximum magnitude of the potential reduction in the p_u caused by the asymmetry of the ground; therefore, a relatively conservative (as small as possible) $p_{u,design}$ can be obtained when χ_p is taken into account. To investigate the numerical relationship between χ_p and the parameters B/d_{50} and C_u, a MLR machine learning model is trained. The dataset from 242 sets of DEM simulations in 9 test groups (D1, D2-U1, D2-U2(1), D2-U3-C2, and D3) is utilized. Each test group corresponds to a unique combination of B/d_{50} and C_u, with only one χ_p value obtained per test group. Consequently, only 9 groups of data could be extracted from these DEM simulation results for the training and testing of the MLR model for χ_p. Given the small size of data, the full set of 9 groups of data is used to train the MLR model, and uncertainty analysis is ultimately conducted on the MLR prediction results using the same 9 groups of data. The following explicit expression of χ_p is attained as

$$\chi_p = 0.0035\left(B/d_{50}\right) + 0.0585C_u + 0.5188, \qquad \chi_p \in (0,1) \tag{6}$$

It is noted that the training dataset is restricted to the following ranges: $B/d_{50} \in [20.83, 41.67]$ (with B=20mm), $C_u \in [1.25, 2.67]$, $C_c \approx 1$, and $\mu = \mu_r = 0.5$. Owing to the constraints of computational resources for DEM simulations, the current χ_p has been fitted only using data within a relatively limited range of gradation parameters. It is anticipated that with an increase of computational resources in the future, the range of parameter values adopted for DEM simulations can be further expanded—for instance, to large B/d_{50} values (corresponding to smaller particle sizes and a greater number of particles) or larger C_u values.

The uncertainty analysis of the regression coefficients is conducted using ordinary least squares (OLS) regression (via the Statsmodels library), and the uncertainty analysis of the predicted results is conducted with error propagation theory (via the Uncertainties library). The uncertainties (signified by the standard errors, SEs) of each coefficient in the OLS regression results are presented in Table **6**. Taking the B/d_{50} as an example, 0.0035 represents the regression-derived coefficient (or point estimate, PE); 0.0006 denotes the SE, reflecting the degree of sampling fluctuation in the estimate (*i.e.*, the uncertainty of the estimation). The relative error (RE) is calculated as: (SE / PE) × 100%, which is used to measure the relative fluctuation of the estimated value. It is seen from Table **6** that the maximum value of RE is 17.14%, which indicates that there exists a certain degree of uncertainty in the current estimation of the coefficients. The underlying reason is that only a relatively limited set of 9 groups of data is utilized to train the MLR model.

Table 7:   Confidence Intervals (CIs) of the Predicted Values of χ_p

B/d_{50}	C_u	χ_p		SE	95% CI		
		Actual	Predicted		Lower bound	Upper bound	Width
20.8	1.25	0.660	0.665	0.030	0.606	0.724	0.118
	1.76	0.680	0.695	0.032	0.632	0.758	0.125
	2.67	0.771	0.748	0.037	0.675	0.821	0.145
31.3	1.25	0.700	0.702	0.034	0.635	0.769	0.133
	1.76	0.745	0.732	0.035	0.663	0.801	0.137
	2.67	0.769	0.785	0.039	0.709	0.861	0.153
41.7	1.25	0.751	0.739	0.037	0.666	0.812	0.145
	1.76	0.762	0.768	0.039	0.692	0.844	0.153
	2.67	0.818	0.822	0.043	0.738	0.906	0.169

Subsequently, based on the coefficient uncertainties, the uncertainties of the predicted values are calculated via the error propagation theory, and the confidence intervals (CIs) of the predicted values are tabulated in Table **7**. In the table, the CI refers to the probability interval that contains the true value of χ_p at a 95% confidence level. Its calculation is based on the assumption that 'predicted values follow a normal distribution', with the formula: predicted value ± (1.96 × SE of predicted value), where 1.96 is derived from the probabilistic characteristics of the normal distribution and is a universal standard for calculating 95% CIs in statistics. In the standard normal distribution, approximately 95% of the probability is concentrated within the range of ±1.96 standard deviations from the mean. As observed in Table **7**, the SEs of the predicted values are from 0.030 to 0.043, and the widths of the CIs range from 0.118 to 0.169. The CI width is not narrow, indicating that there is a certain degree of uncertainty in the predicted values. Analyzing the sources of this uncertainty, in addition to the small amount of data used for model training, the 'actual χ_p values' are derived from DEM simulation results, rather than the 'true values' with absolute zero error, and their inherent uncertainties may also lead to deviations. Meanwhile, the 9 groups of data are further used for testing the MLR model, and the results show that the coefficient of determination (R^2) is 0.930 (> 0.9) and the root mean square error (*RMSE*) is 0.013, which verifies the model has a certain level of overall fitting accuracy and predictive robustness, and can be used for the quantitative prediction and analysis of χ_p.

Figure **16**(**a**) and (**b**) illustrate the variation of the calculated χ_p (the 'Actual' values in the figures) with particle gradation parameters B/d_{50} and C_u, respectively, and the calculated χ_p can also be found in Table **5**. The χ_p values obtained from the MLR model are also plotted in Figure **16**. From Figure **16**(**a**), it is

clearly seen that for a constant C_u, χ_p decreases as d_{50} increases (or as B/d_{50} decreases), while for a constant B/d_{50}, χ_p increases with the increase of C_u. In other words, it may be concluded that small χ_p (with the value about 0.66) can be attained when the mean particle size d_{50} is large and the particle sizes are close to uniform (*i.e.* $C_u \approx 1$); on the contrary, it is also concluded that when the mean particle size d_{50} is small and the particle sizes are comparatively non-uniform, it may be unnecessary to modify p_u calculated based on the continuum mechanics, as χ_p is close to 1.0. Additionally, it is observed from Figure **16** that the explicit expression derived from the MLR model provides an acceptable fitting accuracy to the 'actual' values. For the nine predicted values of χ_p, the average value for the absolute value of deviation is 1.44%. Hence, Eq.(6) can be utilized to calculate χ_p for specific gradation parameters (B/d_{50} and C_u). It is noticed that in studies on the reduction of p_u due to the asymmetry of ground, the primary focus should be on the relative relationship between particle size and footing width. Specifically, for the comparatively non-uniform particle sizes (*e.g.*, C_u=2.67), when $B/d_{50} \geq 81.37$, χ_p reaches its upper limit of 1.00, according to Eq.(6). Theoretically, as B/d_{50} continues to increase, the impact of asymmetry of the ground on the reduction of p_u diminishes and can even be neglected. Similarly, when the particle sizes are close (*e.g.*, C_u=1.25), χ_p reaches 1.00 when $B/d_{50} \geq 102.31$. Given χ_p =1.00, Eq.(6) reduces to:

$$\left(B/d_{50}\right)_{\text{threshold}} = -14.750 C_u + 120.750, \quad C_u \in [1.25, 2.67] \quad (7)$$

when applying Eq.(7), the threshold value of B/d_{50} can be determined based on the given value of C_u, indicating the transition point at which no reduction on p_u is necessary. If the B/d_{50} of the actual soil exceeds the threshold value, the reduction of p_u calculated by the continuum method due to the effect of particle
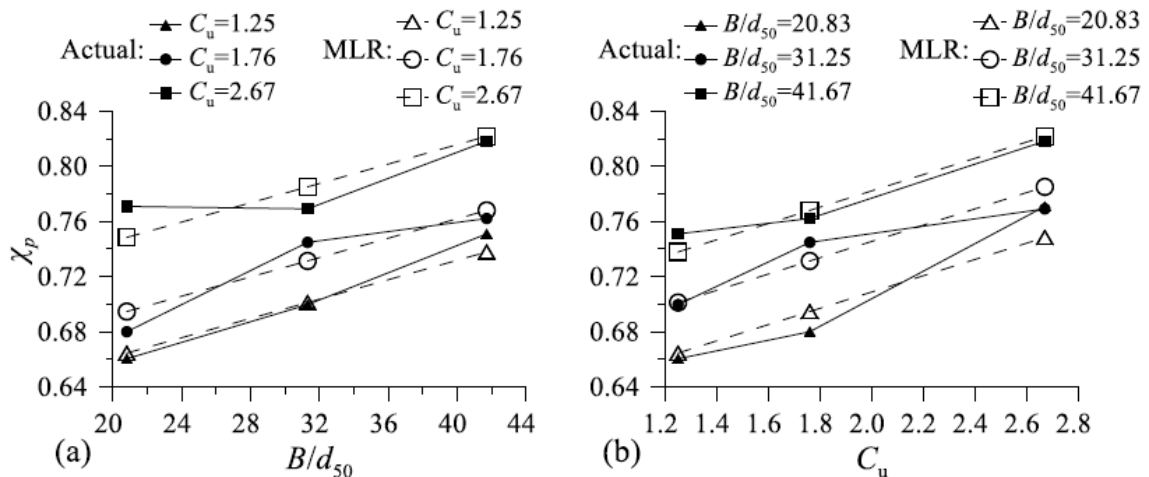

Figure 16: Actual values and MLR model values of χ_p, varying with particle gradation parameters: (a) χ_p versus B/d_{50}; (b) χ_p versus C_u.

gradation becomes unnecessary; if the B/d_{50} of the actual soil is below the threshold value, however, the reduction of p_u shall be appropriately evaluated.

4. MACHINE LEARNING-BASED PREDICTION ON ULTIMATE GROUND BEARING CAPACITY

4.1. Brief Introduction to Machine Learning Models

Since p_u is a function of the gradation parameters (B/d_{50}, C_u, C_c) and the strength parameters (μ, μ_r) apart from the unit weight of the soil particles, the input parameters (B/d_{50}, C_u, C_c, μ, μ_r) are utilized as the features in the training process of ML, while the output parameter p_u is utilized as the label. By defining a set of input parameters along with the output p_u as a sample, three popular machine learning models, namely MLR, ANN and XGBoost, are applied to predicting p_u. The MLR model is a ML model with comparatively simple structure but with the ability of providing explicit expression for p_u, so that the effects of various features on p_u can be readily assessed. The MLR model, nevertheless, is incapable of capturing the potential nonlinear relationship between the input and the output. Compared to the MLR model, the ANN and XGBoost models have more powerful fitting capabilities as they can capture potential nonlinear relationships. It is emphasized that because both ANN and XGBoost belong to the 'black box' models, the relationships between the features and labels established by the two models can't be explicitly presented; as a result, it is not easy to directly analyze the importance of each feature or the influence of each feature on p_u.

A total of 427 test data of ground bearing capacity from DEM simulations, whose statistics are summarized in Table **4** and Table **5** respectively, are shuffled and randomly divided into a portion of 80% as the training dataset and the remaining portion of 20% as the testing dataset. Stratified sampling is performed during this process, meaning that the same proportion of samples is extracted from each test group. This ensures that the samples in each dataset can more effectively represent all test groups.

4.2. MLR Model for Predicting the Ultimate Ground Bearing Capacity

Based on the MLR model, the explicit expression of p_u (in kPa) is attained

$$p_u = -3.50\left(B/d_{50}\right) + 71.58 C_u + 11.25 C_c + 1090.04\mu + 622.09\mu_r - 421.81 \tag{8}$$

The five input parameters of the MLR model are all dimensionless (including B/d_{50}). The output value (p_u) has a unit of kPa (equivalent to kN/m²) and a dimension of $ML^{-1}T^{-2}$. The five coefficients all have a unit of kPa, thus the equation satisfies the requirement of dimensional consistency. By applying the testing dataset to examining Eq.(8), the scatter plot of predicted values versus actual values is depicted in Figure **17**.
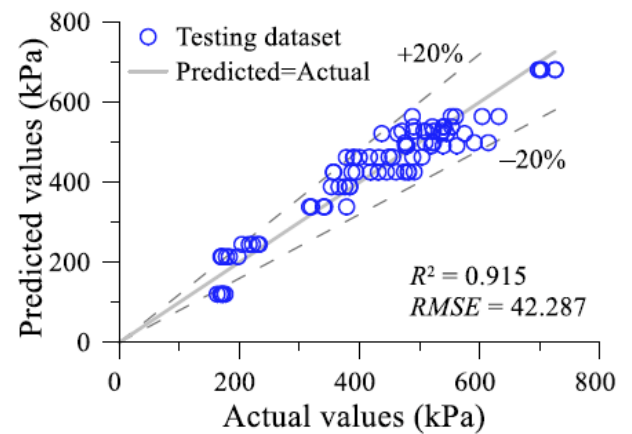

Figure 17: Scatter plot of predicted values of the trained MLR model versus actual values in the testing dataset.

It is clearly observed from Figure **17** that the scattered dots are basically distributed within the range of ±20% about the 45° line where the predicted value equals to the actual value. Based on the testing dataset, the measures of R^2=0.915 (>0.9) and $RMSE$=42.287 implies that the explicit expression/model of p_u can provide an acceptable prediction on p_u. It is noticed in Figure **6**(**b**), however, that there actually exists a nonlinear relationship between p_u and C_u, but the MLR model in Eq.(8) can only supply the linear relationship

Table 8: Sensitivity Ranking of Parameters in the Explicit Expression of p_u Derived from MLR

Parameter	Absolute value of coefficient	Ranking	Absolute value of SC	Ranking (of sensitivity)
B/d_{50}	3.50	5	0.16	4
C_u	71.58	3	0.26	3
C_c	11.25	4	0.02	5
μ	1090.04	1	0.64	1
μ_r	622.09	2	0.48	2

between the input (or feature) and the output. The coefficients in Eq.(8) are influenced by the value ranges of the input parameters, and thus cannot be directly compared (for example, a large coefficient for μ may result from the small value range of μ itself). This makes it impossible to directly derive the sensitivity ranking of parameters (*i.e.*, the extent to which changes in a parameter cause significant fluctuations in p_u). To evaluate the sensitivity of each parameter, the sensitivity ranking of the MLR model parameters is calculated using the Statsmodels library. The core approach is to compute the standardized coefficients (SCs), which eliminate the dimensional differences among parameters: the larger the absolute value of a SC, the stronger the sensitivity of the corresponding parameter to the output p_u. The SC of an input parameter is calculated as: SC = Coefficient of the parameter × (Standard deviation of the parameter / Standard deviation of p_u). The absolute value of SC directly corresponds to the strength of sensitivity.

As observed in Table **8**, the two rankings of the strength parameters μ and μ_r are significantly higher than those of the particle gradation parameters, which is consistent with physical logic: the sliding friction between particles (reflected by μ) directly determines the shear strength of the soil and serves as the core control parameter for bearing capacity; the rolling resistance (reflected by μ_r, analogous to the angularity of particles) enhances overall stability by restricting particle rotation, and its influence on p_u is approximately 75% of that of μ (=(0.48/0.64)×100%), making it also an indispensable key parameter. Among the particle gradation parameters, C_u exhibits the highest sensitivity, as an increase in the span of gradation strengthens interlocking between particles. For B/d_{50}, although its absolute value of coefficient ranks 5th, its sensitivity ranks 4th—this reversal in ranking clearly demonstrates that the original coefficients only reflect 'the impact of a 1-unit change in a parameter on p_u' without accounting for the value range of the parameter itself. Specifically, although

B/d_{50} has a 'small per-unit impact' (3.50 kPa per unit), it has a large actual variation range (from 20.83 to 41.67, a variation of 20.84 units), resulting in a total impact magnitude of 3.50×20.84 = 72.94 kPa; in contrast, C_c has a 'large per-unit impact' (11.25 kPa per unit) but a small actual variation range (from 0.51 to 2.01, a variation of 1.5 units), leading to a total impact magnitude of only 11.25×1.5 = 16.875 kPa. Therefore, changes in B/d_{50} have a greater impact on p_u than C_c, and the SCs precisely capture this 'true intensity of influence'. According to the research of Toyosawa *et al.* (2013), the influence of B/d_{50} can be explained to a certain extent. The thickness of the shear band in the ground varies largely under the influence of d_{50}; when d_{50} is large compared with the footing width B (*i.e.*, when B/d_{50} is small), the p_u of the ground may be affected by the formation of shear bands—a phenomenon referred to as the 'particle size effect'.

It should be noted that the current prediction results are only valid within the value ranges of the parameters considered in this study. For example, the relationship between p_u and C_u may actually be nonlinear; thus, as C_u exceeds the current value range, the prediction deviation of the MLR model may increase, rendering the model predictions no longer applicable. Another example is that C_c generally corresponds to good gradation continuity only when it is between 1 and 3. Since the current study only considers C_c up to 2, the existing p_u prediction may also become inapplicable as C_c continues to increase.

4.3. ANN Model for Predicting the Ultimate Ground Bearing Capacity

The training strategy of ANN model consists of determination of hyperparameters, selection of activation functions, optimization algorithm and loss function and preventing overfitting (*e.g.* Zhang *et al.*, 2021; Zhang *et al.*, 2022). The flowchart of the training of an ANN model, as depicted in Figure **18**, comprises the data preprocessing, model construction,

Table 9: Involved Methods and Characteristics of Components in an ANN Model

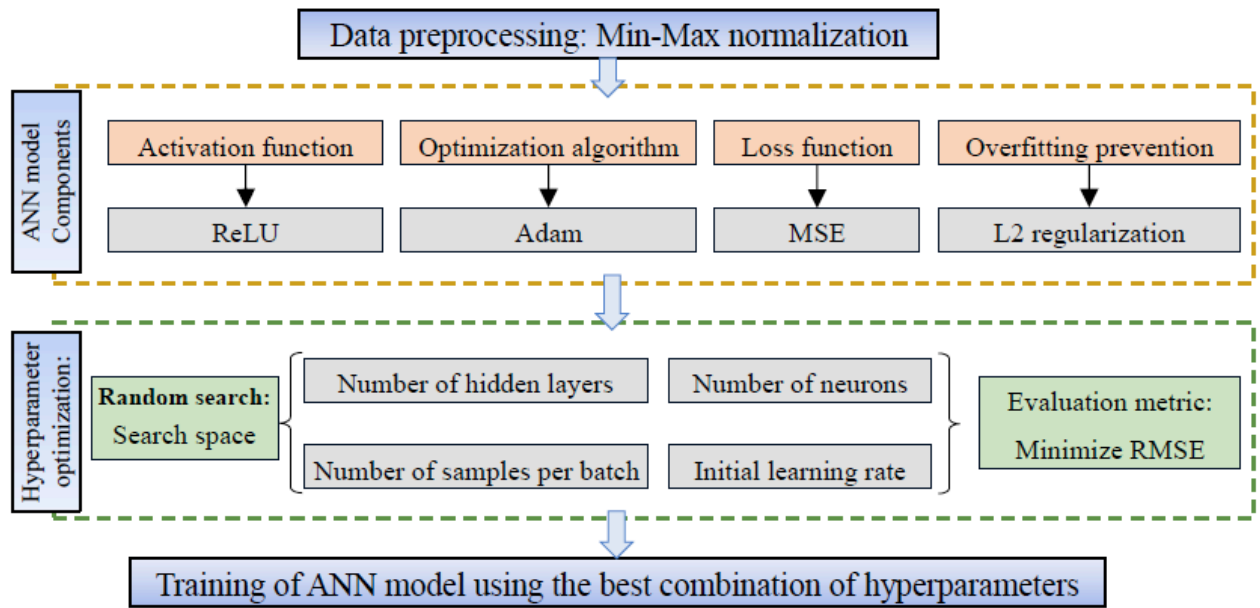| Component	Involved Methods	Characteristic
Data preprocessing	Min-Max normalization	Standardize the numerical range of all features to [0,1].
Activation function	Rectified Linear Unit (ReLU), ReLU(x)=max(0, x)	Mitigates gradient vanishing, computationally efficient (*e.g.* Zhang *et al.*, 2021).
Optimization algorithm	Adaptive Moment estimation (Adam)	Adaptive learning rate, low memory usage (*e.g.* Kingma and Ba, 2014).
Loss Function	Mean Squared Error (*MSE*)	Commonly used in regression tasks to measure error between predicted and actual values.
Overfitting prevention	L2 regularization	Prevents overfitting and enhances generalization.
Hyperparameter optimization	Random Search	Effective for continuous variables, high computational efficiency.

Figure 18: Flowchart of training an ANN model.

hyperparameter optimization and model training. The components of an ANN model and the characteristics of the involved methods are tabulated in Table **9**.

Since the initial learning rate is a continuous variable, the random search method (*e.g.* Bergstra and Bengio, 2012) is adopted here. Owing to the limitation of the size of datasets for ML, the *K*-fold cross-validation (CV) (*e.g.* Dong, 2024) is combined with the random search method to reducing the evaluation bias caused by the data splitting in the ANN model.

Figure **19** illustrates the principle of the combined random search and *K*-fold CV, with '*K*' (=5 in this study) denoting the number of groups of training dataset being split into after shuffling of data. Based on the 50 combinations of random hyperparameters, $\overline{RMSE}$ varies in the range of [38.58, 451.30], with an average value of 100.00 and a standard deviation of 116.27, while the optimal combination of hyperparameters corresponding to the minimum value of $\overline{RMSE}$, as given in the last column in Table **10**, is selected for the ANN model. Then, using the entire training dataset and the optimal hyperparameters, a final ANN model is

trained and tested on the testing dataset.

Figure **20** shows the training results of the ANN model. It is observed from Figure **20**(**a**) that the loss function (*MSE*) gradually approaches smaller values as the training epochs increase. It is seen from Figure **20**(**b**) that the scattered dots are basically distributed within the range of ±20% about the 45° line where the predicted value equals to the actual value. The evaluation measure R^2 of ANN (*i.e.* 0.946) is larger than the value of R^2 (*i.e.* 0.915) obtained by MLR, with a 3.4% increase, while the *RMSE* for the ANN (*i.e.* 33.610) is smaller than *RMSE* of the MLR (*i.e.* 42.287), with a 20.5% decrease, indicating that the ANN model is superior to MLR in prediction accuracy.

Different from MLR, however, the ANN model can't provide an explicit expression owing to its characteristic of 'black box'. To address this limitation and analyze the importance of each feature to p_u, two approaches are utilized. In the approach of permutation importance (PI) (*e.g.* Huang *et al.*, 2016), the values of each feature are randomly shuffled, and then the impact of shuffling on the loss function (*MSE*) is assessed. If the random shuffling of values of a feature

Table 10: Search Space and Results of Random search for Hyperparameters of the ANN Model

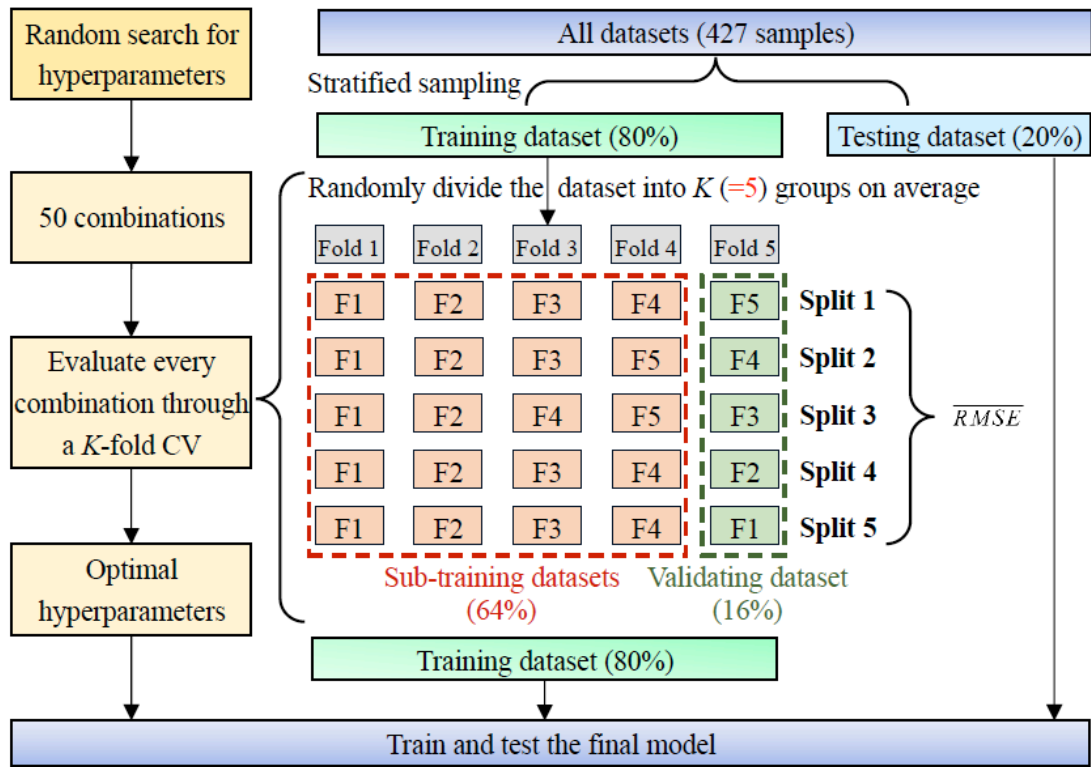| Hyperparameter	Search Space	Search Results
Number of hidden layers	{1, 2, 3, 4, 5}	4
Number of neurons per layer	{5, 6, 7, …, 24, 25}	For each layer: 14, 10, 20, 7
Number of samples per batch	{10, 15, 20, 25}	20
Initial learning rate	$[10^{-4} \sim 10^{-1}]$ (logarithmic sampling)	8.47×10^{-3}

Figure 19: Principle of the random search for hyperparameters and *K*-fold CV of the ANN model.
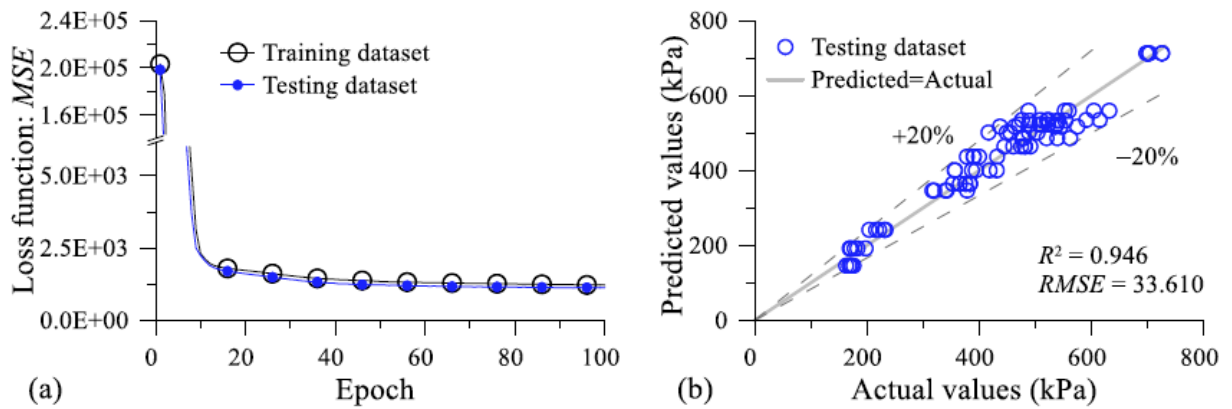

Figure 20: Results of the ANN model: (**a**) *MSE*-epoch curve; (**b**) Scatter plot of predicted values versus actual values for the testing dataset.
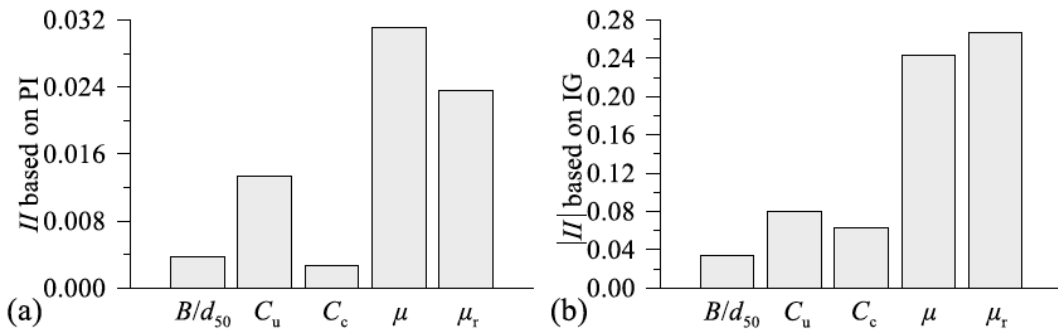
leads to a significant change in *MSE*, this feature shall be important for the prediction of p_u, and hence the change of absolute value of *MSE* is taken as an importance indicator (*II*). The second is the approach of integrated gradient (IG) (*e.g.* Sundararajan *et al.*, 2017). IG is an advanced feature attribution technique specifically designed to provide deep explanations for complex ML models, such as neural networks. It offers insights into model decisions by quantifying the contribution of individual features to the model output.

The importance indicators and ranks of features in the ANN model calculated using two approaches are tabulated in Table **11**, and the corresponding

histograms are plotted in Figure **21**. As a comparison, the linear fitting coefficients and ranks of absolute values of coefficients of the MLR model are also provided in Table **11**. It is seen from Figure **21** that the ranks of feature importance of the ANN model by applying the two approaches are slightly similar. Specifically, no matter which approach is applied, μ and μ_r are the major influential factors of p_u, followed by C_u, while the B/d_{50} and C_c are minor influential factors, and particularly it is interesting to note that the rank of absolute values of linear fitting coefficients for those features of the MLR model also exhibits the similar phenomenon. Additionally, the importance indicator of B/d_{50} obtained by the approach of IG is negative, with

Table 11: Importance Analysis of Features of MLR Model and ANN Model in Predicting p_u

Feature	MLR		ANN			
	linear fitting coefficient	Rank of absolute value	PI		IG	
			II	Rank	*II*	Rank of absolute value
B/d_{50}	−3.52	5	0.0038	4	−0.034	5
C_u	71.55	3	0.0134	3	0.080	3
C_c	10.95	4	0.0027	5	0.062	4
μ	1073.45	1	0.0311	1	0.243	2
μ_r	617.06	2	0.0236	2	0.267	1

Figure 21: Importance indicator (*II*) of features of ANN model in predicting p_u: (**a**) Based on the approach of PI; (**b**) Absolute value based on the approach of IG.

the same sign as the coefficient obtained by MLR, indicates that B/d_{50} has a diminishing effect on the prediction of p_u.

4.4. XGBoost Model for Predicting the Ultimate Ground Bearing Capacity

The XGBoost library is used for training the XGBoost model. The Min-Max normalization method is added in the program for data preprocessing. The L2 regularization is added to enhance the model's generalization ability and prevent overfitting. The partitioning of dataset, the random search for hyperparameters (50 times), and the *K*-fold CV (*K*=5) for the XGBoost model are identical to those employed in the ANN model, as plotted in Figure **19**. Using the entire training dataset and the optimal hyperparameters (as given in the last column in Table

12), a final XGBoost model is trained and tested on the testing dataset.

The training results of XGBoost are plotted in Figure **22** with the loss function (*MSE*) curve in Figure **22**(**a**) and the scatter plot of predicted versus actual values in Figure **22**(**b**). The R^2 of the XGBoost model is 0.950, which is larger than the value of R^2 (*i.e.* 0.915) obtained by MLR, with a 3.8% increase, indicating the slight superiority of XGBoost model to MLR model in prediction accuracy, while the *RMSE* for the XGBoost (*i.e.* 32.501) is smaller than *RMSE* of the MLR (42.287), with a 23.1% decrease. Similar to ANN models, XGBoost can't provide an explicit expression for p_u, so the built-in feature importance (FI) approach in the XGB library and the SHapley Additive exPlanations values of tree ensembles (TreeSHAP) approach (*e.g.* Lundberg *et al.*, 2018) may be employed for analyzing

Table 12: Search Space and Results of Random search for Hyperparameters of the XGBoost Model

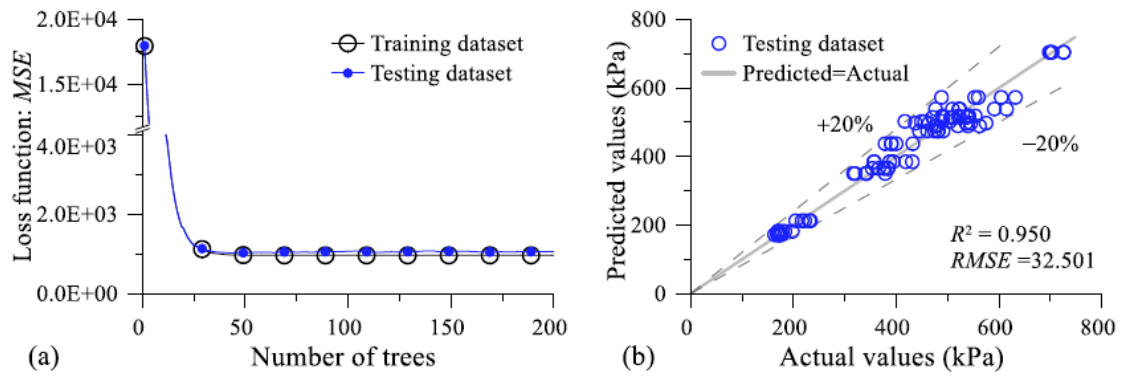| Hyperparameter	Search space	Search results
Number of estimators (trees)	{100, 200, 300}	200
Maximum tree depth	{3, 4, 5, 6, 7, 8}	6
Minimum child weight	{1, 2, 3, 4, 5 ,6}	1
Subsample ratio	[0.5~1.0] (uniform sampling)	0.81
Column sample ratio per tree	[0.5~1.0] (uniform sampling)	0.78
Learning rate	[10^{-4}~10^{-1}] (logarithmic sampling)	0.11

Figure 22: Results of the XGBoost model: (**a**) *MSE*-number of trees curve; (**b**) Scatter plot of predicted values versus actual values for the testing dataset.

the importance of features on p_u. In the approach of FI, there are three importance indicators (*II*), namely *II* by Weight (II_W), *II* by Gain (II_G), and *II* by Cover (II_C). II_W represents the number of times a feature is used to split samples across all trees, which relates to its contribution to the final prediction. II_G reflects the average benefit or improvement brought by a feature when used for splitting. II_C represents the number of samples affected by the splitting nodes where a feature is used. The approach of SHAP was originally developed from game theory and is used to measure the contribution of variables to a prediction. XGBoost can automatically utilize the TreeSHAP algorithm, which is optimized for tree-based models within the SHAP library.

Table **13** and Figure **23** display the importance indicators (*II*) of features based on the approaches of FI and TreeSHAP in XGBoost. Generally, II_G is considered the most critical indicator in the approach of FI, as it directly measures the extent to which a feature improves the model's predictive performance. Based on II_G in Figure **23**, it is concluded that μ and μ_r are the most critical parameters for predicting p_u, followed by C_u, while the B/d_{50} and C_c are minor influential factors. This conclusion is further supported by the feature importance ranks obtained from the Tree SHAP method, which shows similar results. Additionally, this aligns with the findings from the MLR and ANN models.

Among the three models, the value of MLR is the smallest, while the value of XGBoost is the largest, by

Table 13: Importance Indicators (*II*) of Features of XGBoost Model in Predicting p_u

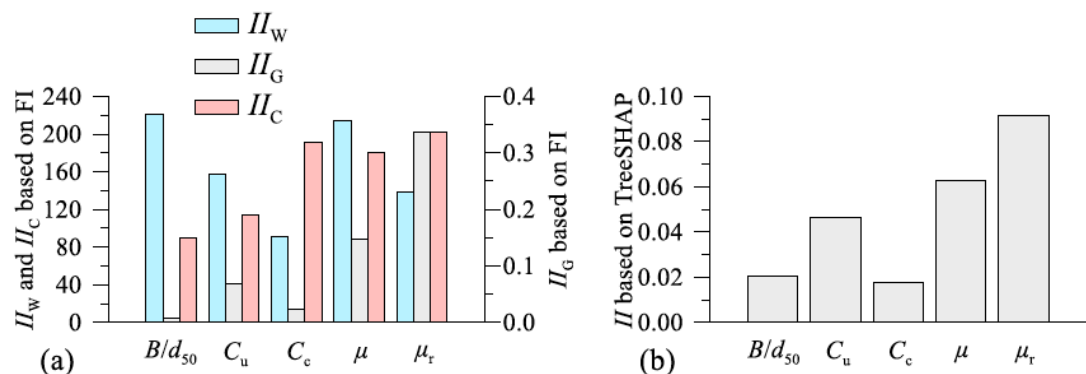| Feature	FI						TreeSHAP	
	II_W	Rank	II_G	Rank	II_C	Rank	II	Rank
B/d_{50}	221	1	0.0085	5	89.3	5	0.0204	4
C_u	157	3	0.0695	3	114.7	4	0.0462	3
C_c	91	5	0.0230	4	190.6	2	0.0176	5
μ	214	2	0.1478	2	180.2	3	0.0627	2
μ_r	139	4	0.3364	1	201.9	1	0.0913	1

Figure 23: Importance indicators (*II*) of features of XGBoost model in predicting p_u: (a) Based on the approach of FI; (b) Based on the approach of TreeSHAP.

means of the measure of R^2; while the value of MLR is the largest, and the value of XGBoost is the smallest, by means of the measure of *RMSE*. The superiority of MLR model is that it can provide an explicit expression of p_u with clear implications between different input parameters (B/d_{50}, C_u, C_c, μ, μ_r) and p_u, while the superiorities of ANN and XGBoost lie in that they may offer the nonlinear relationship and better accuracy models for p_u.

5. CONCLUSION

Unlike continuum-based methods, the DEM can capture the influence of granular characteristics (such as the particle gradation, particle friction, and particle shape) on the ultimate ground bearing capacity p_u. In a total of 432 DEM tests, the rolling resistance linear contact model is employed to predict the ultimate bearing capacity of ground of graded soils (with the gradation parameters of mean particle size d_{50}, coefficient of uniformity C_u, and coefficient of curvature C_c and the strength parameters of friction coefficient μ and rolling resistance coefficient μ_r). The objective is to assess the impact of these granular characteristics on the asymmetric development of ground failure pattern (or shear band) and p_u under the vertical concentrated loading. The modern tool of machine learning is used to train a prediction model for the p_u of the ground using datasets obtained from a large amount of DEM simulations. Some valuable observations and conclusions are summarized as follows:

1. The ultimate ground bearing capacity p_u increases with C_u, C_c, μ, and μ_r, but decreases with B/d_{50} (for a constant footing width B). The shear band thickness increases with d_{50} or C_u. A negative correlation is observed between p_u and the corresponding footing rotation angle α_u.

2. A modification factor χ_p for the p_u predicted by continuum-based methods is defined and an explicit expression of χ_p is derived using the MLR model. A larger d_{50} and smaller C_u may lead to a lower χ_p, indicating a more evident overestimation of continuum-based methods on p_u.

3. The MLR machine learning model provides an explicit expression for the prediction of p_u, while the 'black-box'-style ANN and XGBoost models achieve higher prediction accuracy. Feature importance analysis shows the ranking of input parameter influences on p_u (from highest to lowest): μ and μ_r > C_u > B/d_{50} and C_c.

AUTHOR CONTRIBUTIONS

All authors contributed to the study conception and design. Numerical simulation, data collection and analysis were performed by Xi Chen, Zongqi Liu and Zuokai Zhang. The first draft of the manuscript was written by Xi Chen and all authors commented on previous versions of the manuscript. All authors read and approved the final manuscript.

DATA AVAILABILITY

The data that support the findings of this study are available from the corresponding author, Zongqi Liu, upon reasonable request.

DECLARATIONS

Conflict of Interest

Xi Chen, Zongqi Liu, Zuokai Zhang, Chenlu Wang, Liusheng Cui, Zhikai Yan, Zhe Xu, Saif Ullah, Fengkai Ge, Fengwei Li declare that they have no conflict of interest.

REFERENCES

[1]   Azami A, Pietruszczak S, Guo P (2010) Bearing capacity of shallow foundations in transversely isotropic granular media. Int J Numer Anal Methods Geomech 34(8): 771-793. https://doi.org/10.1002/nag.827

[2]   Behera RN, Patra C (2018) Ultimate bearing capacity prediction of eccentrically inclined loaded strip footings. Geotech Geol Eng 36:3029-3080. https://doi.org/10.1007/s10706-018-0521-z

[3]   Bergstra J, Bengio Y (2012) Random search for hyper-parameter optimization. J Mach Learn Res 13(2).

[4]   Bhandari A, Han J (2009) DEM study of a shallow foundation under vertical loading. In: Contemporary Topics in Ground Modification, Problem Soils, and Geo-Support. pp 465-472. https://doi.org/10.1061/41023(337)59

[5]   Chen X, Wu Y, Yu Y *et al.* (2014) A two-grid search scheme for large-scale 3-D finite element analyses of slope stability. Comput Geotech 62:203-215. https://doi.org/10.1016/j.compgeo.2014.07.010

[6]   Chen X, Wang D, Yu Y *et al.* (2020) A modified Davis approach for geotechnical stability analysis involving non-associated soil plasticity. Géotechnique 70(12): 1109-1119. https://doi.org/10.1680/jgeot.18.P.158

[7]   Chen X, Tang J, Cui L *et al.* (2023) Stability and failure pattern analysis of bimslope with Mohr-Coulomb matrix soil: From a perspective of micropolar continuum theory. J Cent South Univ 30(10): 3450-3466. https://doi.org/10.1007/s11771-023-5452-z

[8]   Chen X, Liu Z, Cui L, Tang J (2022) An automatic identification method for width of shear band of sand in PFC simulations. Chin J Geotech Eng 44(S2): 179-182.

[9]   Dong Z, Li P, Yao M, Li X, Zhao L, Wang L (2024) Comparison and analysis of denoising method in TBM key

tunnelling data. Georisk Assess Manag Risk Eng Syst Geohazards: 1-14.

[10] Fathipour H, Payan M, Chenari RJ *et al.* (2022) General failure envelope of eccentrically and obliquely loaded strip footings resting on an inherently anisotropic granular medium. Comput Geotech 146: 104734. https://doi.org/10.1016/j.compgeo.2022.104734

[11] Fu Z, Chen S, Liu S (2016) Discrete element simulations of shallow plate-load tests. Int J Geomech 16(3): 04015077. https://doi.org/10.1061/(ASCE)GM.1943-5622.0000588

[12] Gao Z, Lu D, Du X (2020) Bearing capacity and failure mechanism of strip footings on anisotropic sand. J Eng Mech 146(8): 04020081. https://doi.org/10.1061/(ASCE)EM.1943-7889.0001814

[13] Huang N, Lu G, Xu D (2016) A permutation importance-based feature selection method for short-term electricity load forecasting using random forest. Energies 9(10): 767. https://doi.org/10.3390/en9100767

[14] Jiang M, Konrad JM, Leroueil S (2003) An efficient technique for generating homogeneous specimens for DEM studies. Comput Geotech 30(7): 579-597. https://doi.org/10.1016/S0266-352X(03)00064-8

[15] Kimura T, Kusakabe O, Saitoh K (1985) Geotechnical model tests of bearing capacity problems in a centrifuge. Géotechnique 35(1): 33-45. https://doi.org/10.1680/geot.1985.35.1.33

[16] Kingma DP, Ba J (2014) Adam: A method for stochastic optimization. arXiv preprint arXiv:1412.6980.

[17] Krabbenhoft S, Damkilde L, Krabbenhoft K (2014) Bearing capacity of strip footings in cohesionless soil subject to eccentric and inclined loads. Int J Geomech 14(3): 04014003. https://doi.org/10.1061/(ASCE)GM.1943-5622.0000332

[18] Krishnan K, Chakraborty D (2022) Probabilistic study on the bearing capacity of strip footing subjected to combined effect of inclined and eccentric loads. Comput Geotech 141: 104505. https://doi.org/10.1016/j.compgeo.2021.104505

[19] Li J, Tian Y, Cassidy MJ (2015) Failure mechanism and bearing capacity of footings buried at various depths in spatially random soil. J Geotech Geoenviron Eng 141(2): 04014099. https://doi.org/10.1061/(ASCE)GT.1943-5606.0001219

[20] Liu Z, Chen X, Cui L, Tang J (2024) Porosity field measurement technique for shear band width in direct shear and biaxial discrete element numerical experiments. Rock Soil Mech 45(S1): 742-750.

[21] Liu Z, Chen X, Cui L, Xu Z, Yan Z (2025) Numerical analysis of the effect of the gradation characteristics of soil particles on the ground bearing capacity of a rigid footing via the discrete element method. J Cent South Univ, In Press.

[22] Loukidis D, Chakraborty T, Salgado R (2008) Bearing capacity of strip footings on purely frictional soil under eccentric and inclined loads. Can Geotech J 45(6): 768-787. https://doi.org/10.1139/T08-015

[23] Lundberg SM, Erion GG, Lee SI (2018) Consistent individualized feature attribution for tree ensembles. arXiv preprint.

[24] Lyu Y, Chen X, Tang J *et al.* (2023) Application assessment of hybrid smoothed finite element method for geotechnical deformation and stability analysis. J Cent South Univ 30(3): 919-933. https://doi.org/10.1007/s11771-023-5285-9

[25] Lyu Y, Chen X, Tang J *et al.* (2024) An implicit stabilized node-based smoothed finite element method for ultimate bearing capacity analysis of strip footing. Eng Anal Bound Elem 160: 52-64. https://doi.org/10.1016/j.enganabound.2023.12.018

[26] Pan Q, Chen X, Zhang J, Li F, Zhang D, Tang C (2024) Preface for machine learning and artificial intelligence in geotechnics: Opportunities and challenges. J Cent South Univ 31: 3819-3822. https://doi.org/10.1007/s11771-024-5842-x

[27] Rattez H, Shi Y, Sac-Morane A *et al.* (2022) Effect of grain size distribution on the shear band thickness evolution in sand. Géotechnique 72(4): 350-363. https://doi.org/10.1680/jgeot.20.P.120

[28] Roy N, Shree K (2024) Machine learning prediction tool for seismic bearing capacity of strip footings in rock mass. Transp Infrastruct Geotech 11(2): 900-919. https://doi.org/10.1007/s40515-023-00312-3

[29] Shiau JS, Lyamin AV, Sloan SW (2003) Bearing capacity of a sand layer on clay by finite element limit analysis. Can Geotech J 40(5): 900-915. https://doi.org/10.1139/t03-042

[30] Sundararajan M, Taly A, Yan Q (2017) Axiomatic attribution for deep networks. In: International Conference on Machine Learning. PMLR, pp 3319-3328.

[31] Tang J, Wang X, Chen X *et al.* (2022) Geotechnical Strain Localization Analysis Based on Micropolar Continuum Theory Considering Evolution of Internal Characteristic Length. Int J Geomech 22(8): 06022016. https://doi.org/10.1061/(ASCE)GM.1943-5622.0002462

[32] Tang J, Chen X, Cui L, Liu Z (2023) Strain localization of Mohr-Coulomb soils with non-associated plasticity based on micropolar continuum theory. J Rock Mech Geotech Eng 15(12): 3316-3327. https://doi.org/10.1016/j.jrmge.2023.02.029

[33] Tang J, Chen X, Cui L, Xu Z, Liu G (2024) Geotechnical analysis involving strain localization of overconsolidated soils based on unified hardening model with hardening variable updated by a composite scheme. Int J Numer Anal Methods Geomech 48(8): 2237-2256. https://doi.org/10.1002/nag.3730

[34] Thapa A, Adhikari K, Shrestha D K, *et al.* (2025) Deep Learning-Assisted Computational Modeling of Granular Soil Behavior for Foundation Design Optimization in Kharke Khola Region. Int. J. Geoinformatics 1(2): 25-45. https://doi.org/10.46610/IJGST.2025.v01i02.003

[35] Toyosawa Y, Itoh K, Kikkawa N, Yang J, Liu F (2013) Influence of model footing diameter and embedded depth on particle size effect in centrifugal bearing capacity tests. Soils Found 53(2): 349-356. https://doi.org/10.1016/j.sandf.2012.11.027

[36] Veiskarami M, Shokoohi MA (2023) A Lower Bound Estimate of the Bearing Capacity of Foundations on Inherently Anisotropic Sands Implementing the Fabric Tensor. Geotech Geol Eng 41(2): 831-845. https://doi.org/10.1007/s10706-022-02308-1

[37] Wang D, Chen X, Yu Y *et al.* (2019) Stability and deformation analysis for geotechnical problems with nonassociated plasticity based on second-order cone programming. Int J Geomech 19(2): 04018190. https://doi.org/10.1061/(ASCE)GM.1943-5622.0001339

[38] Wu P, Chen J, Huang J, *et al.* (2026) Calibration of Mesoscopic Parameters for Lunar Soil Using a Machine Learning-Based Discrete Element Method. J. Aerosp. Eng. 39(1): 04025110. https://doi.org/10.1061/JAEEEZ.ASENG-6267

[39] Wu Y, Zhou X, Gao Y *et al.* (2020) Bearing capacity of embedded shallow foundations in spatially random soils with linearly increasing mean undrained shear strength. Comput Geotech 122: 103508. https://doi.org/10.1016/j.compgeo.2020.103508

[40] Xiao Y, Zhao M, Zhao H *et al.* (2018) Finite element limit analysis of the bearing capacity of strip footing on a rock mass with voids. Int J Geomech 18(9): 04018108. https://doi.org/10.1061/(ASCE)GM.1943-5622.0001262

[41] Yin Z, Wang P (2021) Micro-mechanical analysis of caisson foundation in sand using DEM: particle shape effect. Appl Ocean Res 111: 102630. https://doi.org/10.1016/j.apor.2021.102630

[42] Zhang P, Yin Z, Jin Y (2021) State-of-the-art review of machine learning applications in constitutive modeling of soils. Arch Comput Methods Eng 28(5): 3661-3686. https://doi.org/10.1007/s11831-020-09524-z

[43]   Zhang P, Yin Z, Jin Y (2022) Machine learning-based modelling of soil properties for geotechnical design: review, tool development and comparison. Arch Comput Methods Eng: 1-17. https://doi.org/10.1007/s11831-021-09615-5